DOI: 10.61782/fa.2025.0770

FORUM ACUSTICUM
EURONOISE 2025

SHIP PROPELLER NON-CAVITATING NOISE IN NON-UNIFORM FLOW

Maël Brun[1*] **Samuel Pinson**[1] **Justine Carpentier**[1] **Jacques-André Astolfi**[1]
[1] IRENav EA 3634, BCRM Brest, École Navale C600, 29240 Brest Cedex 9

ABSTRACT

The mitigation of underwater noise from ships is a matter of concern as it significantly impacts the behaviour and communication of marine fauna, as well as the acoustic discretion of military ships. The ship-radiated underwater noise is a complex acoustic source in which several components radiate sound at the same time. Among them, the propeller itself involves different coupled phenomena. This communication focuses on the non-cavitating component of the propeller noise which can be described with acoustic analogies. It consists in modelling the acoustic pressure field as a sum of three source terms. First, monopoles model the sound produced by the propeller blade water displacement and is referred as the thickness noise. Then, dipoles model the sound due to forces applied on the blades by the flow and is referred as the loading noise. Finally, quadrupoles model water turbulences. This study aims at comparing the thickness noise with the loading noise in the context of a non-uniform flow. To do so, the flow is decomposed into a uniform flow in the propeller disk and a non-uniform flow due the axial velocity fluctuations.

Keywords: *Acoustic analogy, Ship noise, Non-cavitating noise, Non-uniform flow*

1. INTRODUCTION

Cargo-ship traffic noise is of growing concern [1] due to its impacts on marine fauna [2]. It is also of interest for acoustic discretion of military ships. Therefore, providing simple models to understand each acoustic source involved in the ship radiated sound along with experimental results [3] is useful. Main contributors are machinery through hull vibrations and propeller noise. The propeller noise contribution itself can be decomposed into cavitation noise, thickness noise and loading noise. Even though the non-cavitating phenomena contribute less to the radiated sound, their effect remains interesting [4, 5], especially under the influence of a non-uniform inflow.

So in a first approximation, only the non-cavitating propeller is considered here. Acoustic analogies and integral formulations are applied to evaluate those acoustic sources due to the fluid motion around the propeller. These methods allow to consider the blade thickness effect (monopole source type), the loading on the blade (dipole source type) as well as turbulences (quadrupole source type) [6] and interactions with moving solid boundaries [7, 8]. Usually, numerical models first rely on computational fluid dynamics (CFD) then combined with analytically calculated acoustic pressure field in a post-processing stage [9] with acoustic analogies. Despite being accurate, these models can be difficult to interpret and not necessarily accessible, especially to perform parametric studies over the propeller characteristics. Results in a non-uniform inflow also widely depend on the meshing strategies [10]. To avoid this, thickness noise and loading noise can be described with Fourier series expansions [11] which allows to take into account the inflow non-uniformity with the angular direction of the blade [12, 13]. Other parameters of the blade such as its shape [14] can also be described with the modal decomposition.

In order to get a simple analytical result, another approach is applied in this study. It consists in approximating the propeller blades by moving point sources. These sources are characterised by a mass injection rate to describe the thickness effect of one blade section

*Corresponding author: mael.brun@ecole-navale.fr.

and concentrated external forces applied to this section. The quadrupole terms describing the turbulences around the blades are neglected. The pressure field is deduced from the convective wave equation [8, 15] with only the two acoustic sources remaining: the thickness and loading noises. The case of a single-screw cargo ship is examined. The non-uniform flow due to standard axial velocity fluctuations is then taken into account in the sources expressions. The goal of this model is to explain the impact of the non-uniform flow on the near-field and far-field acoustic radiation. Levels on the direction of the hull are deduced to evaluate its influence.

In section 2, the non-cavitating sound pressure field resulting from the thickness noise and the loading noise is deduced from the moving point source model with non-uniform flow. In section 3, a parametric study is performed from which the conclusions are summarized in section 4.

2. NON-CAVITATING SOUND PRESSURE FIELD OF A PROPELLER

In order to measure the acoustic radiation from the propeller, the relative location of the observer to the centre of the propeller disk is constant. While it rotates, both the propeller and the observer on point O move at the same time in the uniform flow. One way to extend Lighthill's acoustic analogy to uniformly moving media is to consider the convective wave equation [8].

2.1 Solving the convective wave equation

Propeller rotating blades can be approximated by moving point sources [16]. In this case, analytical formulas can be obtained with straightforward calculations. The convective wave equation can be solved by applying the Ffowcs Williams and Hawkings (FW-H) analogy [17] which provides the acoustic pressure anywhere around the propeller moving surface. The blades are described by points located at 70% of their radius R. These equivalent acoustic sources of the analogy (fig.1) are simply defined by a mass injection rate $Q(t)$ (corresponding to the blade thickness noise) and a force term $f_i(t)$ (corresponding to the blade loading noise composed of the lift $\boldsymbol{L}$ and drag $\boldsymbol{D}$). In the linear approximation, the resulting pressure field consists in the sum of identical point sources modelling each blade. A single source which accounts for one blade is considered. Forces are applied at location $\boldsymbol{x_s}(t)$. Then

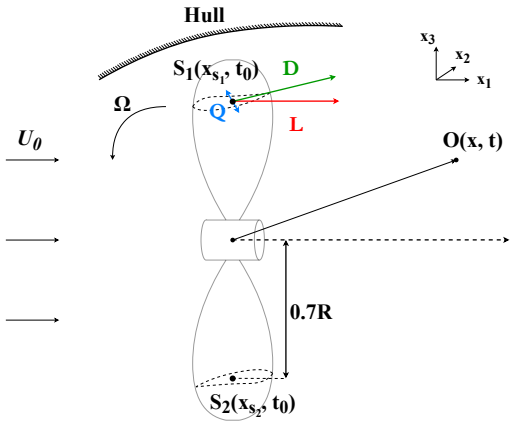

Figure 1. Geometry of the problem. Blades are represented by point sources with lift L, drag D and mass injection rate Q. Observer is at point O.

the general equation governing the pressure field is

$$\frac{1}{c_\infty}\frac{D^2p}{Dt^2} - \frac{\partial^2 p}{\partial x_i^2} = -\frac{\partial}{\partial x_i}.\{f_i(t)\delta(\boldsymbol{x}-\boldsymbol{x_s}(t))\} + \frac{D}{Dt}\{Q(t)\delta(\boldsymbol{x}-\boldsymbol{x_s}(t))\}, \tag{1}$$

where the summation convention applies. Its solution is the convolution of the right-hand side with the Green's function G defined by:

$$\frac{1}{c_\infty^2}\frac{D^2G(\boldsymbol{x},t\,|\,\boldsymbol{y},t_0)}{Dt^2} - \frac{\partial^2 G(\boldsymbol{x},t\,|\,\boldsymbol{y},t_0)}{\partial x_i^2} = \delta(\boldsymbol{x}-\boldsymbol{y})\delta(t-t_0), \tag{2}$$

where c_∞ is the water sound speed and

$$\frac{D}{Dt} = \frac{\partial}{\partial t} + U_{0_i}.\frac{\partial}{\partial x_i}, \tag{3}$$

$\boldsymbol{U_0}$ being an arbitrary vector of the uniform flow speed, $\boldsymbol{x}$ the location of the observer at time t and $\boldsymbol{y}$ the location of the source at time t_0. To solve eq.2, let us consider the same Green function in the coordinate system of the fluid at rest with the change of variable

$$\begin{cases} \boldsymbol{\xi} = \boldsymbol{x} - \boldsymbol{U_0}t \\ \boldsymbol{\eta} = \boldsymbol{y} - \boldsymbol{U_0}t_0 \end{cases}, \tag{4}$$

so that $G'(\boldsymbol{\xi},t\,|\,\boldsymbol{\eta},t_0) = G(\boldsymbol{x},t\,|\,\boldsymbol{y},t_0)$ which simplifies eq.2 into a non-convective wave equation:

$$\frac{1}{c_\infty}\frac{\partial^2 G'}{\partial t^2} - \frac{\partial^2 G'}{\partial \xi_i^2} = \delta(\boldsymbol{\xi}-\boldsymbol{\eta})\delta(t-t_0), \tag{5}$$

for which the solution is

$$G'(\boldsymbol{\xi}, t \mid \boldsymbol{\eta}, t_0) = \frac{\delta\left(t - t_0 - \frac{|\boldsymbol{\xi}-\boldsymbol{\eta}|}{c_\infty}\right)}{4\pi \mid \boldsymbol{\xi} - \boldsymbol{\eta} \mid}. \tag{6}$$

Changing back to the original coordinates

$$G(\boldsymbol{x}, t \mid \boldsymbol{y}, t_0) = \frac{\delta\left(t - t_0 - \frac{|\boldsymbol{r}|}{c_\infty}\right)}{4\pi \mid \boldsymbol{r} \mid}, \tag{7}$$

where $\boldsymbol{r} = \boldsymbol{x} - \boldsymbol{y} - \boldsymbol{U_0}(t - t_0)$. The uniform flow is now considered only along the x_1-axis as shown in fig.1. The loading noise pressure field p_L is deduced by calculating the space and time convolution of the Green's function in eq.7 and the external force source term in eq.1 as follows

$$p_L(\boldsymbol{x}, t) = -\frac{\partial}{\partial x_i} \cdot \left\{ \frac{f_i(\tau)}{4\pi \mid \boldsymbol{r} \mid D_s} \right\}, \tag{8}$$

where

$$\tau = t - \frac{\mid \boldsymbol{r} \mid}{c_\infty}, \tag{9}$$

and

$$\boldsymbol{r} = \boldsymbol{x} - \boldsymbol{x_s}(\tau) - \boldsymbol{U_0}(t - \tau). \tag{10}$$

The present calculation takes into account the Doppler effects due to both the uniform flow and the motion of the rotating point source which depends on $\boldsymbol{V_s}(\tau)$ and $\boldsymbol{\Gamma_s}(\tau)$ (respectively the velocity and acceleration of the point source $\boldsymbol{x_s}(\tau)$). The coefficients

$$D_s = 1 - \frac{\boldsymbol{V_s} - \boldsymbol{U_0}}{c_\infty} \cdot \frac{\boldsymbol{r}}{\mid \boldsymbol{r} \mid}, \tag{11}$$

and

$$D_0 = 1 + \frac{\boldsymbol{U_0}}{c_\infty} \cdot \frac{\boldsymbol{r}}{\mid \boldsymbol{r} \mid}, \tag{12}$$

describe the influence of higher Mach numbers. The contribution of the loading noise to the pressure field is then obtained by calculating the derivative in eq.8:

$$p_L(\boldsymbol{x}, t) = \frac{r_i}{4\pi c_\infty D_s^2 \mid \boldsymbol{r} \mid} \cdot \left[\frac{f_i'(\tau)}{\mid \boldsymbol{r} \mid} + \frac{f_i(\tau)}{c_\infty D_s} \frac{\boldsymbol{\Gamma_s} . \boldsymbol{r}}{\mid \boldsymbol{r} \mid^2} + f_i(\tau) \left(\boldsymbol{V_s} - \boldsymbol{U_0} \left(1 - \frac{D_s}{D_0} \right) \right) \cdot \frac{\boldsymbol{r}}{\mid \boldsymbol{r} \mid^3} \right], \tag{13}$$

which reduces to

$$p_L(\boldsymbol{x}, t) = \frac{r_i}{4\pi c_\infty \mid \boldsymbol{r} \mid^2} \cdot \left[f_i'(\tau) + \frac{f_i(\tau)}{c_\infty} \frac{\boldsymbol{\Gamma_s} . \boldsymbol{r}}{\mid \boldsymbol{r} \mid} \right], \tag{14}$$

in the far-field approximation and at low Mach numbers. Likewise, the thickness noise contribution is

$$p_T(\boldsymbol{x}, t) = \frac{1}{4\pi D_s^2} \left[\frac{Q'(\tau)}{\mid \boldsymbol{r} \mid} + \frac{Q(\tau)}{c_\infty D_s} \frac{\boldsymbol{\Gamma_s} . \boldsymbol{r}}{\mid \boldsymbol{r} \mid^2} + Q(\tau) \left(\boldsymbol{V_s} - \boldsymbol{U_0} \left(1 - \frac{D_s}{D_0} \right) \right) . \frac{\boldsymbol{r}}{\mid \boldsymbol{r} \mid^3} \right], \tag{15}$$

which reduces to

$$p_T(\boldsymbol{x}, t) = \frac{1}{4\pi \mid \boldsymbol{r} \mid} \left[Q'(\tau) + \frac{Q(\tau)}{c_\infty} \frac{\boldsymbol{\Gamma_s} . \boldsymbol{r}}{\mid \boldsymbol{r} \mid} \right], \tag{16}$$

in the far-field approximation and at low Mach numbers.

2.2 Simulated propeller parameters

To implement eq.13 and eq.15, the cargo-ship propeller parameters are chosen from ref. [3] and summarized in tab.1. The forces are applied to a blade section at 70% of the radius as shown in fig.1. To get a realistic order of magnitude for the sources, this section geometry is considered equivalent to a hydrofoil with chord length w from which the mean thickness l is deduced. The chord length w is considered to be 60 % of the radius. The lift and drag coefficients (C_L and C_D) are chosen for an angle of attack $\alpha_0 = 5°$,

$$\begin{cases} C_L(\alpha_0) \simeq 0.55 \\ C_D(\alpha_0) \simeq 0.011 \end{cases}.$$

Table 1. Simulated cargo ship propeller characteristics.

R	Radius [m]	2.45
Z	Number of blades [Ø]	4
l	Mean thickness at $0.7R$ [m]	0.12
w	Width at $0.7R$ [m]	1.47
S	Projected wing area [m^2]	3.6
Ω	Rotation speed [rpm]	150
U_0	Mean flow [$m.s^{-1}$]	8

The acoustic sources are then evaluated. In a uniform flow, the source terms are not time-dependent. The mass injection rate which characterises the thickness noise is

$$Q = \rho R l \sqrt{(0.7R\Omega)^2 + U_0^2}, \tag{17}$$

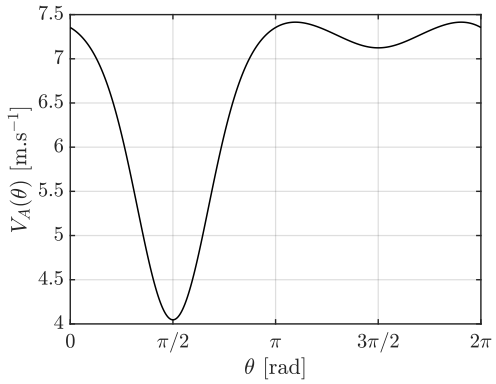

Figure 2. Axial velocity as the location $\boldsymbol{x_s}(t)$ of the point source corresponding to the first blade starting at $\theta = 0$ rad. It minimizes when the source is closer to the hull.

with ρ the water mass density and U_0 the modulus of the uniform flow all along the x_1-axis. The forces which characterise the loading noise are

$$L, D = \frac{1}{2}\rho\left[(0.7R\Omega)^2 + U_0^2\right] SC_{L,D}(\alpha_0), \tag{18}$$

where the angle of attack remains constant at $\alpha_0 = 5°$ in the uniform-flow case.

2.3 Influence of the axial velocity fluctuations

Let us consider a non-uniform velocity field in the propeller disk. The closer the source to the hull, the lower the propeller inflow due to boundary layer effects. This behaviour is reproduced from the typical wake field for a single-screw cargo ship. To account for the blade width averaging effect, the convolution of this typical wake field and a rectangular shape provides the filtered non-uniform velocity field presented in fig.2. The resulting velocity field is then included in eq.17 and eq.18 to evaluate its influence on the now time-dependent mass injection rate

$$Q(\tau) = \rho Rl\sqrt{(0.7R\Omega)^2 + V_A(\theta(\tau))^2}, \tag{19}$$

and forces

$$L, D(\tau) = \frac{1}{2}\rho\left[(0.7R\Omega)^2 + V_A(\theta(\tau))^2\right] SC_{L,D}(\alpha(\tau)), \tag{20}$$

where

$$\theta(\tau) = \Omega\tau + \phi_0(z), \tag{21}$$

with $\phi_0(z)$ the blade number z angle of origin. The time-dependent angle of attack $\alpha(\tau)$ is

$$\alpha(\tau) = \alpha_0 + \Delta\alpha(\tau) \tag{22}$$

where

$$\Delta\alpha(\tau) = tan^{-1}\left(\frac{U_0}{0.7R\Omega}\right) - tan^{-1}\left(\frac{V_A(\theta(\tau))}{0.7R\Omega}\right). \tag{23}$$

Assuming that, with α expressed in radians,

$$\left.\frac{dC_L}{d\alpha}\right|_{\alpha=\alpha_0} \simeq 2\pi, \tag{24}$$

the time-dependent lift coefficient becomes

$$C_L(\alpha(\tau)) = C_L(\alpha_0) + 2\pi\Delta\alpha(\tau), \tag{25}$$

and the drag coefficient is

$$C_D(\alpha(\tau)) \simeq C_D(\alpha_0). \tag{26}$$

The thickness noise and loading noise in non-uniform inflow are expected to have higher levels as the first term of the sums in eq.14 and eq.16 now also varies in time.

3. PARAMETRIC STUDY

3.1 Near-field *vs* far-field

The non-uniform inflow is first considered so that the mass injection rate is described by eq.19 and the two external forces are described by eq.20. The observer point is fixed in the plane $x_2 = 0$ at $\beta = \pi/4$ (fig.3). Results are compared between a near-field distance ($r_0 = 3$ m) and a far-field distance ($r_0 = 1$ km) in (x_1, x_3) plane. Comparisons are done by compensating the geometric divergence (in dB re 1 μPa @ 1 m). In both cases, the acoustic pressure field is described by eq.13 and eq.15. The time-domain simulation is performed on a fourth of a blade revolution to obtain the Fourier series coefficients.

The resulting spectra (fig.4) emphasize the similar impact of both the thickness noise and the loading noise. The differences between fig. 4 (top) and 4 (bottom) are due to the influence of the last term of eq.13 and eq.15 which varies with $1/|\,\boldsymbol{r}\,|^2$.

Fig.5 shows the fundamental frequency amplitudes as a function of β. The decrease is noticeable for both

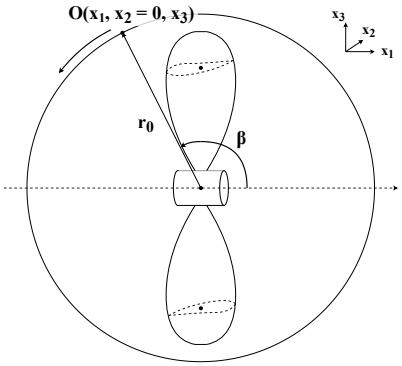

Figure 3. Angular location of the observer in the cross-section for which $x_2 = 0$ to compute the directivity of the propeller. r_0 refers to the constant distance with the centre of the propeller disk.

sources at any direction. The thickness noise tends to radiate more uniformly as the observer distance increases. This change in the directivity pattern justifies the importance of the simulation near to the hull. At $\beta = \pi/2$, the thickness noise prevails on the loading noise with a 54 dB difference in near-field and a 30 dB difference in far-field. At $\beta = 0$, the loading noise prevails on the thickness noise with a 13 dB difference in near-field and far-field. Interestingly, the sound level at $\beta = 0$ or π is not null. This is due to the axial velocity fluctuations (section 3.2).

3.2 Uniform flow *vs* non-uniform flow

The case of the uniform flow is studied by applying eq.17 and 18 rather than eq.19 and eq.20. The spectra obtained in fig.6 underline the predominance of the thickness noise over the loading noise both in near-field and far-field at $\beta = \pi/4$. While the near-field magnitudes for the thickness noise remain the same as for a non-uniform flow in fig.6 (top) and fig.4 (top), the loading noise decreases by 23 dB on average. In the far-field shown in fig.6 (bottom), only the fundamental frequency is relevant. In that case, the thickness noise decreases by 97 dB whereas the loading noise decreases by 140 dB. The effects of the loading noise highly depends on the non-uniformity.

The directivity diagrams obtained in fig.7 compared to fig.5 show the effect of the wake field on the loading noise. The uniform-inflow near-field directivity presented in fig.7 (top) has a different pattern than in fig.5 (top). As

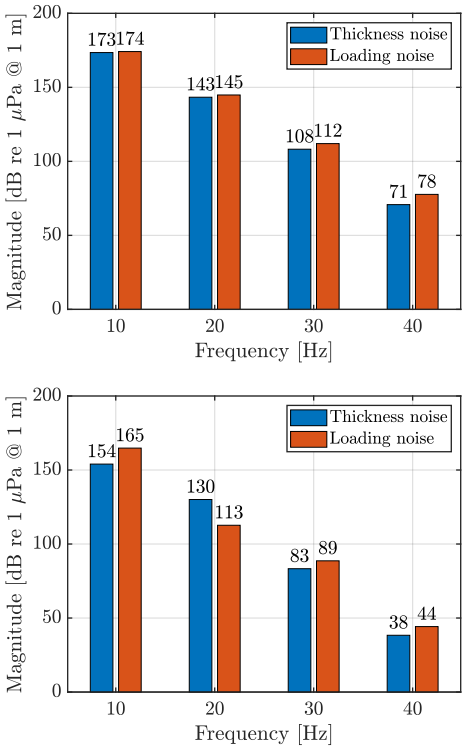

Figure 4. Frequency power spectra in dB re 1 μPa @ 1 m for a non-uniform inflow. Top: near-field spectrum with $r_0 = 3$ m from the centre of the propeller disk centre. Bottom: far-field spectrum at $r_0 = 1$ km.

expected, the uniform-inflow near-field directivity is null at $\beta = 0$ or π. The magnitude of the loading noise radiating in the direction of the hull $\beta = \pi/2$ remains high with 195 dB. The uniform-inflow far-field directivity presented in fig.7 (bottom) also presents a different pattern than in fig.5 (bottom). The non-uniform-inflow far-field higher levels are due to the time derivative of f_i and Q in eq.13 and eq.15.

3.3 Influence of the external force direction

Drag force changes the direction of the force vector applied and must impact the directivity pattern of the propeller. $C_D = 0$ is fixed so that only a lift force along the x_1-axis is applied to the rotating blade section. The directivity diagram obtained for the uniform flow in the far-field in fig.8 now shows a symmetry around x_3-axis compared to fig.7 (bottom). The propeller no longer radi-

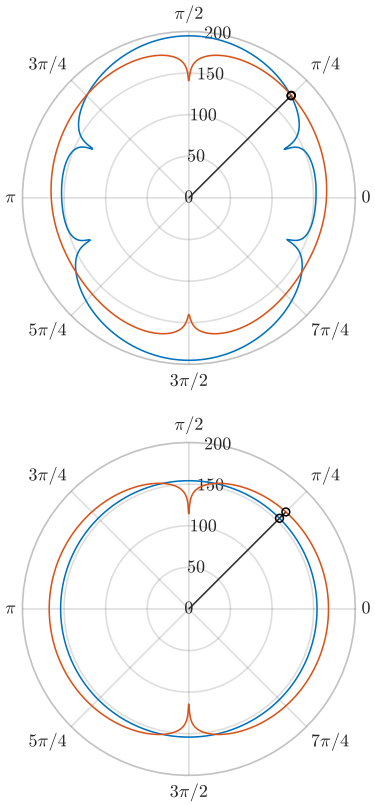

Figure 5. Directivity in the (x_1, x_3) plane in dB re 1 μPa @ 1 m, the blue and red curves respectively corresponding to thickness noise and loading noise. Top: near-field + non-uniform flow + lift and drag forces. Bottom: far-field + non-uniform flow + lift and drag forces. Lines point out the location of the observer for the Fourier series expansion in fig.4.

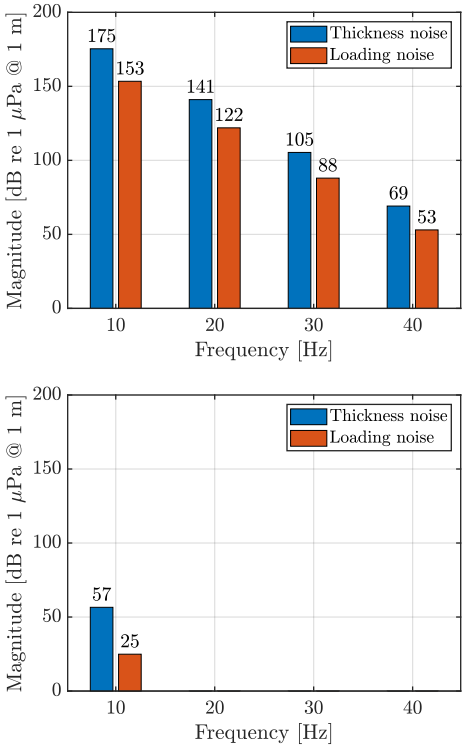

Figure 6. Frequency power spectra in dB re 1 μPa @ 1 m for a uniform inflow. Top: near-field spectrum with $r_0 = 3$ m from the centre of the propeller disk centre. Bottom: far-field spectrum at $r_0 = 1$ km.

ates along the x_3-axis as presented in fig.8 because forces only apply along x_1. This last comparison emphasizes the importance of the force orientations on the directivity pattern. Thus, the force repartition of a real propeller blade would imply a different directivity pattern.

4. CONCLUSION

The simple time-domain propeller model presented in this paper allows to decompose the complex nature of the propeller radiated sound. It permits to implement the non-uniform inflow due to the ship hull. Simplifying the physical phenomena at stake helps to understand their impact on the acoustic pressure field. To do so, the simplification consisted in modelling the blades by moving point sources characterised by a mass injection rate and concentrated forces.

In the uniform flow, the thickness noise prevails on the loading noise which is no longer the case for the non-uniform flow. Comparison between near-field and far-field levels at 1 m (with compensated geometric divergences) shows that the near-field is significantly stronger than the far-field (except for some local minima in the directivity pattern). This might be of importance in future work to study the hull vibro-acoustic interaction with the ship's propeller.

Moreover, a much more realistic analytical model could include the blade geometry and the non-uniform

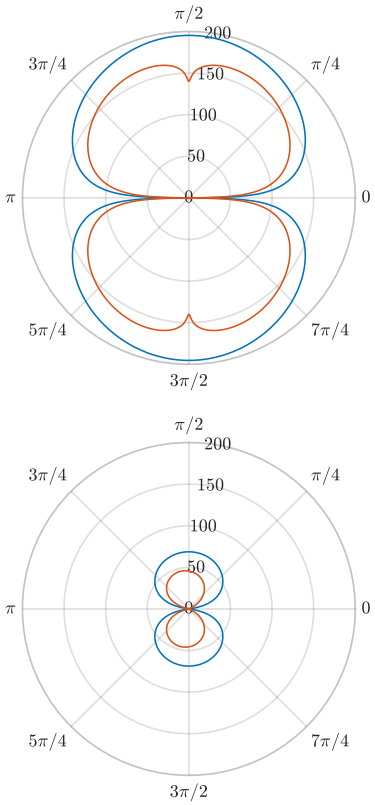

Figure 7. Directivity in the (x_1, x_3) plane in dB re 1 μPa @ 1 m, the blue and red curves respectively corresponding to thickness noise and loading noise. Top: near-field + uniform flow + lift and drag forces. Bottom: far-field + uniform flow + lift and drag forces.

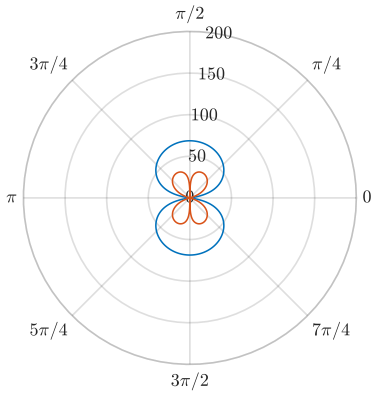

Figure 8. Directivity in the (x_1, x_3) plane in dB re 1 μPa @ 1 m, the blue and red curves respectively corresponding to thickness noise and loading noise. far-field + uniform flow + lift force only.

flow by integration over the propeller disk where the propeller and the inflow can be decomposed into Fourier series [11, 13]. These models may be improved by using a better description of a non-uniform inflow with an unsteady random component, and a more realistic blade geometry.

5. REFERENCES

[1] E. Cruz, T. Lloyd, J. Bosschers, F. H. Lafeber, P. Vinagre, and G. Vaz, "Sounds: Status of underwater noise from shipping - study on inventory of existing policy, research and impacts of continuous underwater noise in europe," research report, WavEC Offshore Renewables and Maritime Research Institute Netherlands, 2021.

[2] C. Erbe, S. A. Marley, R. P. Schoeman, J. N. Smith, L. E. Trigg, and C. B. Embling, "The effects of ship noise on marine mammals - a review," *Front. Mar. Sci*, vol. 6, p. 606, 2019.

[3] P. T. Arveson and D. J. Vendittis, "Radiated noise characteristics of a modern cargo ship," *J. Acoust. Soc. Am.*, vol. 107, no. 1, pp. 118–129, 2000.

[4] H. Seol, B. Jung, J.-C. Suh, and S. Lee, "Prediction of non-cavitating underwater propeller noise," *J. Sound Vib.*, vol. 257, no. 1, pp. 131–156, 2002.

[5] Y. Wang, U. Göttsche, and M. Abdel-Maksoud, "Sound field properties of non-cavitating marine propellers," *J. Mar. Sci. Eng.*, vol. 8, no. 11, p. 885, 2020.

[6] M. J. Lighthill, "On sound generated aerodynamically i. general theory," *Proc. R. Soc. Lond. A*, vol. 211, no. 1107, pp. 564–587, 1952.

[7] J. E. Ffowcs Williams and D. L. Hawkings, "Sound generation by turbulence and surfaces in arbitrary motion," *Philoso. Trans. R. Soc. Lond. A*, vol. 264, no. 1151, pp. 321–342, 1969.

[8] M. Goldstein, "Unified approach to aerodynamic sound generation in the presence of solid boundaries," *J. Acoust. Soc. Am.*, vol. 56, no. 2, pp. 497–509, 1974.

[9] F. Porcacchia, G. Dubbioso, R. Muscari, and C. Testa, "Effects of flow incidence on propeller underwater radiated noise," *Phys. Fluids*, vol. 37, no. 1, p. 017154, 2025.

[10] J. Kimmerl, P. Mertes, and M. Abdel-Maksoud, "Application of large eddy simulation to predict underwater noise of marine propulsors. part 2: Noise generation," *J. Mar. Sci. Eng.*, vol. 9, no. 7, p. 778, 2021.

[11] S. Zhong, P. Zhou, R. Fattah, and X. Zhang, "A revisit of the tonal noise of small rotors," *Proc. R. Soc. A*, vol. 476, no. 2244, pp. 1–21, 2020.

[12] D. B. Hanson, "Sound from a propeller at angle of attack: A new theoretical viewpoint," *Proc. R. Soc. Lond. A*, vol. 449, no. 1936, pp. 315–328, 1995.

[13] H. Jiang, S. Zhong, H. Wu, X. Zhang, X. Huang, G. Zhou, and B. Chen, "Radiation modes of propeller tonal noise," *J. Vib. Acoust.*, vol. 144, no. 2, p. 021009, 2021.

[14] I. E. Garrick and C. E. Watkins, "A theoretical study of the effect of forward speed on the free-space sound-pressure field around propellers," research report NACA-TR-1198, NASA, 1954.

[15] X. Gloerfelt, *Bruit rayonné par un écoulement affleurant une cavité : simulation aéroacoustique directe et application de méthodes intégrales*. Phd thesis, École Centrale de Lyon, 2001.

[16] R. Stuff, "Noise field of a propeller with angular inflow," *AIAA J.*, vol. 26, no. 7, pp. 777–782, 1988.

[17] G. Ghorbaniasl, L. Siozos-Rousoulis, and C. Lacor, "A time-domain kirchhoff formula for the convective acoustic wave equation," *Proc. R. Soc. A*, vol. 472, no. 2187, p. 20150689, 2016.